A Deep Learning-Based Approach for Terminal Area Flight Flow Operational Safety Situation Awareness

DENG Cheng, ZHANG Qiqian, ZHANG Honghai, WAN Junqiang, LI Jingyu*

State Key Laboratory of Air Traffic Management System, College of Civil Aviation, Nanjing University of Aeronautics and Astronautics, Nanjing 211106, P. R. China

(Received 30 September 2024; revised 26 November 2024; accepted 10 December 2024)

Abstract: Safety is the cornerstone of the civil aviation industry and the enduring focus of civil aviation. This paper uses air traffic complexity and potential aircraft conflict relationships as entry points to study the operational safety level of terminal area flight flows and proposes a deep learning-based method for safety situation awareness in terminal area aircraft operations. Firstly, a more comprehensive and precise safety situation assessment features are constructed. Secondly, a deep clustering situation recognition model with added safety situation information capture layer is proposed. Finally, a spatiotemporal graph convolutional neural network based on attention mechanism is constructed for predicting safety situations. Experimental results from a real dataset show that: (1) The proposed model surpasses traditional models across all evaluated dimensions; (2) the recognition model ensures that the encoded features capture distinctive safety situation information, thereby enhancing model interpretability and task alignment; (3) the prediction model demonstrates superior integrated modeling capabilities in both spatial and temporal dimensions. Ultimately, this paper elucidates the spatiotemporal evolution characteristics of air traffic safety situation levels, offering valuable insights for air traffic safety management.

Key words: air traffic; safety situation awareness; deep learning; safety management

CLC number: U8 **Document code:** A **Article ID:** 1005-1120(2024)06-0783-23

0 Introduction

Currently, the contradiction between the continuously growing air traffic demand and the insufficient available resources is becoming increasingly prominent, exacerbating the busy nature of air routes and terminal area operations, and intensifying the pressure on air traffic control. Mid-air collision has been identified by the International Civil Aviation Organization as one of the five high-risk events[1]. Air proximity incident is an inevitable step in mid-air collisions, and according to the accident chain principle, preventing air proximity incident can effectively avoid mid-air collisions. Technologies for detecting potential conflicts play a crucial role by providing real-time monitoring of aircraft positions, speeds, and altitudes. This allows for the proactive identification of potential conflicts based on the trajectory vectors of aircraft, thereby aiding in the prevention of air proximity incidents.

The terminal area, linking cruise flight above with takeoff and landing below, is a complex region where the airport surface integrates three-dimensionally with the air route network. This area is characterized by high aircraft maneuverability and traffic density, making it a frequent zone for aircraft conflict incidents. According to the ASRS database, 557 air proximity incidents occurred in the terminal area from 2016 to 2021[2]. Therefore, comprehensively considering the traffic complexity of flight flows (i.e., basic traffic flow parameters and aircraft maneuverability) and the potential conflict relationships among groups of aircraft in the terminal area,

*Corresponding author, E-mail address: zhangqq@nuaa.edu.cn.

How to cite this article: DENG Cheng, ZHANG Qiqian, ZHANG Honghai, et al. A deep learning-based approach for terminal area flight flow operational safety situation awareness[J]. Transactions of Nanjing University of Aeronautics and Astronautics, 2024, 41(6): 783-805.

http://dx.doi.org/10.16356/j.1005-1120.2024.06.009

intelligently assessing the operational safety situation to enhance controllers' situational awareness and support control decision-making is a core technology to eliminate air proximity. This has significant scientific and practical value for ensuring air traffic safety, protecting lives, implementing precise control strategies, and improving air traffic efficiency.

Situation awareness is a concept introduced by Endsley in 1988[3], defined as "within a volume of time and space, the perception of the elements in the environment, the comprehension of their meaning, and the prediction of their status in the near future". He proposed a theoretical model of situation awareness consisting of three stages, which were perception of elements in the environment, comprehension of the current situation, and prediction of future status.In recent years, scholars have conducted extensive research on situation awareness in various air traffic contexts, such as congestion[4-6], complexity[7-9], safety[10-13], and environmental[14] issues, achieving significant results that provide a solid foundation for this study.

In recent years, machine learning has provided new directions for situational awareness issues. Scholars have conducted in-depth research on situational awareness in various scenarios within the air traffic domain. Generally, in the field of machine learning-based situational awareness, scholars have transformed situation recognition into a classification problem and situation prediction into a time series prediction problem. Due to the significant spatiotemporal heterogeneity in air traffic, and with the widespread application of graph convolutional neural networks in recent years, some scholars have converted prediction problems into spatiotemporal sequence prediction problems.

Research outcomes related to the operational safety situational awareness in air traffic primarily focus on two aspects: the micro-level aircraft potential conflict collision risk and the macro-level overall airspace operational risk. Most studies approach the subject from the perspective of potential conflict and collision, utilizing various risk analysis models[15] (including the Reich collision risk model, the potential conflict area-based collision risk model, the position error probability-based collision risk model, the stochastic differential equation-based collision flight model, the event-based collision risk model, and the accident number-based risk analysis model) to study collision risks between aircraft. However, these studies describe air traffic safety situations solely from the perspective of potential conflict events and neglect the complexity of air traffic flight flows. This results in a situational awareness process that lacks a holistic view, thereby limiting the ability to perceive, understand, and predict safety risks.

Therefore, in recent years, some scholars have combined macro-level traffic complexity with micro-level aircraft potential conflicts to study the safety situational awareness of aircraft operations in airspace from the perspective of complex networks. The main approach involves constructing potential conflict situation networks, mining situational representation elements and achieving situational awareness. Being data-driven, it is more capable of revealing the implicit information within the data. Relevant scholars have established potential conflict relationships between aircraft based on methods such as relative physical distance between aircraft[16], ACARS communication distance[17], potential conflict probability and target safety level[11], and three-dimensional velocity obstacle models[18]. They then constructed potential conflict situation networks among aircraft, extract network attributes as situational representation elements, and used traditional clustering algorithms[11], independent component analysis methods[17], and other techniques to identify airspace operational safety situations. Methods like least squares support vector machine (LSSVM)[18] and long short-term memory (LSTM)[19] were employed to predict airspace operational safety situations.

In terms of safety situation element extraction, existing research often focuses solely on attributes of the potential conflict network (e.g., average node degree, average strength, average weighted clustering coefficient, network efficiency, network density, etc.) to mine situation representation elements.

This approach tends to overlook the coupling effects of air traffic flow parameters and aircraft maneuverability characteristics on safety situation awareness.

Regarding safety situation recognition, most current studies directly apply clustering algorithms to high-dimensional features. However, the existing research has shown that the performance and efficiency of traditional clustering algorithms significantly decrease in high-dimensional spaces, thus leading to the "curse of dimensionality" problem[20-22], which affects the reliability and scientific validity of safety situation level classification results. Some scholars have combined feature dimensionality reduction algorithms with clustering algorithms to improve the clustering quality. Although the clustering quality can be enhanced, the processes of dimensionality reduction and clustering are independent of each other, and the reduced features may lose the ability to capture safety risk information, thus leading to a mismatch between the goals of dimensionality reduction and clustering.

Furthermore, in the field of safety situation prediction, research indicates significant spatiotemporal heterogeneity in air traffic[14, 23]. Existing studies often consider only the temporal characteristics of safety situation levels and ignore the spatial characteristics caused by airspace structure and flight procedures.

In summary, to address the research gaps in the aforementioned three aspects, this paper proposes a deep learning-based method for safety situation awareness in terminal area aircraft operations as shown in Fig.1. The main contribution can be summarized in four-folds.

(1) Following basic principles of measurability, accessibility, timeliness, and multidimensionality, we construct safety situation assessment feature matrix from three perspectives: basic traffic flow parameters, aircraft maneuverability metrics, and aircraft potential conflict situation network attributes.

(2) Based on an autoencoder deep clustering algorithm, we introduce a safety situation information capture layer and propose a risk-aware deep clustering model (RADCM) to ensure that the dimensionality-reduced features capture distinctive safety situation information, thus achieving precise and efficient classification of safety situation levels.

(3) We incorporate attention based spatial-temporal graph convolutional networks (ASTGCN) to explore the spatiotemporal heterogeneity of safety situations, enabling accurate prediction of safety situation levels.

(4) This paper analyzes the characteristics of terminal area safety levels from three dimensions: the hourly distribution of safety level percentages, the duration of safety levels, and the spatiotemporal evolution of safety levels. It provides data support and reference for air traffic safety management, as-

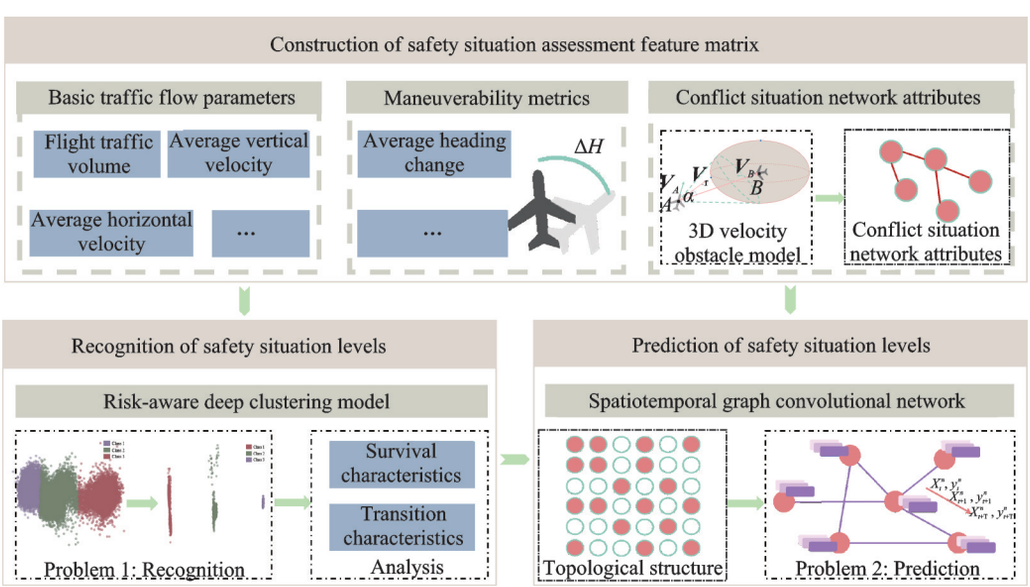

Fig.1 Main research content of safety situation awareness

sisting air traffic control departments in identifying high-risk areas and periods. This, in turn, enables the implementation of targeted measures to enhance safety management at these critical times and locations.

1 Methodology

1.1 Definitions and problem description

Definition 1 Terminal area airspace network G^s

To describe the characteristics of aircraft take-off and landing operations and topological structure of the terminal area airspace, an undirected unweighted graph $G^s=\{V^s,E^s,A^s\}$ is used to represent the terminal area network structure. Here $V^s=\{v_1^s,v_2^s,\cdots,v_N^s\}$ represents the set of sub-airspace nodes within a terminal area, and N denotes the number of sub-airspace nodes in the terminal area; E^s represents the set of edges, indicating connectivity between sub-airspace nodes; $\boldsymbol{A}^s=(a_{ij}^s)\in\mathbf{R}^{N\times N}$ is the adjacency matrix of this network, where $a_{ij}^s=1$ indicates a connection between nodes v_i^s and v_j^s.

Definition 2 Potential conflict relationship

Potential conflict relationship refers to situations in air traffic management where, based on the current position, heading, and speed of aircraft, the future trajectory vectors of two or more aircraft may lead to conflict. It is considered a pre-alert state occurring before an actual conflict arises.

Definition 3 Potential conflict situation time-varying network G_t^p

As shown in Fig.2, the active aircraft at different time slices are used as network nodes, and the potential conflict relationships between aircraft form the edges, thereby constructing an undirected unweighted graph $G_t^p=\{V_t^p,E_t^p,A_t^p\}$ to represent the potential conflict situation network. Here, t represents the tth time slice, $V_t^p=\{v_{t1}^p,v_{t2}^p,\cdots,v_{tM_t}^p\}$ the set of active aircraft nodes, and M_t the number of active aircraft nodes at time t; E_t^p represents the set of edges at time t, indicating potential conflict relationships between active aircraft; $\boldsymbol{A}_t^p=(a_{ij}^p)\in\mathbf{R}^{M_t\times M_t}$ is the adjacency matrix of this network, where $a_{ij}^p=1$ indicates a potential conflict relationship between two active aircraft.

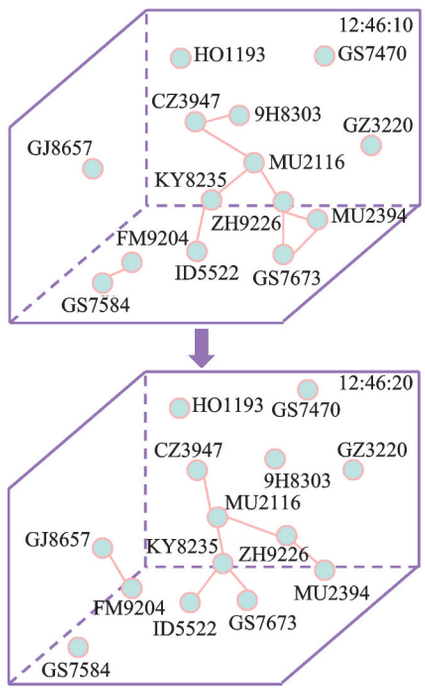

Fig.2 Illustration of potential conflict situational time-varying network

Definition 4 Safety situation assessment feature matrix $\boldsymbol{X}$

As shown in Fig.3, this paper defines the aircraft operation safety situation assessment feature matrix as $\boldsymbol{X}=(\boldsymbol{X}_1,\boldsymbol{X}_2,\cdots,\boldsymbol{X}_S)^{\mathrm{T}}\in\mathbf{R}^{S\times F\times N}$, representing features of all nodes over all time sequences. Here F represents the number of features, N the number of sub-airspace nodes, and S the total number of time sequences. $\boldsymbol{X}_t\in\mathbf{R}^{F\times N}$ represents the metrics matrix at time t.

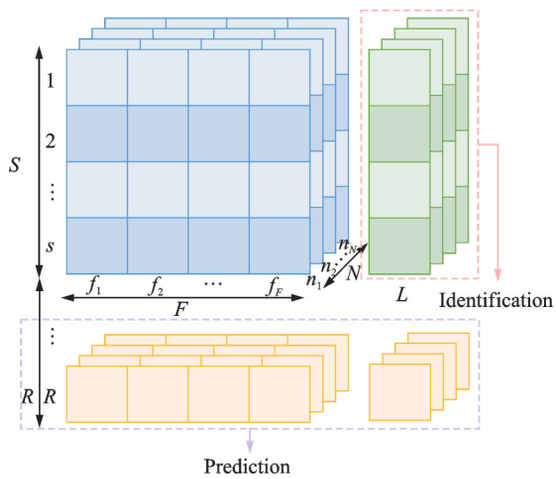

Fig.3 Data structure diagram

Problem description 1 Safety situational awareness

This paper studies the representation of the operational safety level of flight flows in terminal areas based on trajectory operational data by utilizing traffic complexity and potential aircraft conflict relationships.

Problem description 2 Safety situation recognition

This problem can be defined as the quantitative classification of historical air traffic operation states based on the assessment feature matrix representing the safety situation. The core is to establish and train a mapping function f_1 to cluster the safety situation features at different times, thereby obtaining the safety situation levels $\boldsymbol{L}$.

$$[\boldsymbol{X}_1,\boldsymbol{X}_2,\cdots,\boldsymbol{X}_S]^{\mathrm{T}} \xrightarrow{f_1} [(\boldsymbol{X}_1,\boldsymbol{L}_1),(\boldsymbol{X}_2,\boldsymbol{L}_2),\cdots,(\boldsymbol{X}_S,\boldsymbol{L}_S)]^{\mathrm{T}}$$

Problem description 3 Safety situation prediction

This problem can be defined as establishing and training a mapping function f_2 based on the terminal area airspace network $\boldsymbol{G}^{\mathrm{s}}$, historical feature matrix, and historical safety situation levels to predict the safety situation levels for the next R time steps.

$$[(\boldsymbol{X}_1,\boldsymbol{L}_1),(\boldsymbol{X}_2,\boldsymbol{L}_2),\cdots,(\boldsymbol{X}_S,\boldsymbol{L}_S)]^{\mathrm{T}} \xrightarrow{f_2,\boldsymbol{G}^{\mathrm{s}}} [(\boldsymbol{X}_{S+1},\boldsymbol{L}_{S+1}),(\boldsymbol{X}_{S+2},\boldsymbol{L}_{S+2}),\cdots,(\boldsymbol{X}_{S+R},\boldsymbol{L}_{S+R})]^{\mathrm{T}}$$

1.2 Potential conflict situation network construction model

The potential conflict relationships between active aircraft are characterized by their dynamic complexity and non-linearity. By comprehensively considering the three-dimensional spatial position information and flight trajectory data (including heading and speed) of aircraft, this study establishes potential conflict edges through geometric methods to construct the potential conflict situation network. The following two conditions for defining potential conflict edges are proposed.

(1) Using the three-dimensional relative distance between active aircraft as the standard for constructing potential conflict edges has the advantage of being quick and intuitive. When the distance between aircraft is less than the threshold D, it is considered that there is a potential conflict relationship between the two aircraft, forming a potential conflict edge.

(2) Satisfying the velocity obstacle relationship[24]. Firstly, establish an ellipsoidal protection zone, then construct a three-dimensional velocity obstacle region. This region represents all possible velocity vectors that could lead to a collision with the aircraft. Next, determine whether the relative velocity between the two aircraft falls within this obstacle region to assess whether there is a potential conflict between the aircraft. The specific method is as follows.

Step 1 Establishing the ellipsoidal protection zone. In this study, the terminal area is taken as the research object, so a Cartesian coordinate system is established with the airport as the origin, in which the positive Z-axis points upwards, the positive X-axis east, and the positive Y-axis north. Aircraft operating in the airspace must maintain a certain horizontal or vertical separation; therefore, an ellipsoidal protection zone is established to simulate the actual flight state of the aircraft, as shown in Fig.4. Let the coordinates of aircraft in the terminal area be (x_B, y_B, z_B). The ellipsoidal protection zone can be represented as

$$\frac{(X-x_B)^2}{d_{\mathrm{v}}^2}+\frac{(Y-y_B)^2}{d_{\mathrm{v}}^2}+\frac{(Z-z_B)^2}{d_{\mathrm{l}}^2}\leqslant 1 \quad (1)$$

where d_{v} is the semi-major axis of the ellipsoid in the x- and y-axis directions, and d_{l} the semi-major axis of the ellipsoid in the z-axis direction.

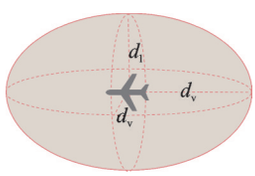

Fig.4 Illustration of ellipsoidal flight protection zone

Step 2 Constructing the three-dimensional velocity obstacle region and determining the existence of potential conflict relationships. As shown in Fig.5, tangents are drawn from the active aircraft $A(x_A, y_A, z_A)$ in the airspace to the sides of the

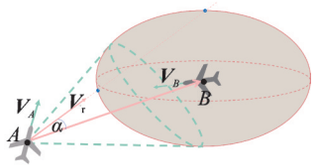

Fig.5 Three-dimensional velocity obstacle model

flight protection zone of aircraft B, forming a three-dimensional velocity obstacle region. The relative velocity $\boldsymbol{V}_r = \boldsymbol{V}_A - \boldsymbol{V}_B$ is then evaluated to determine whether it falls within the three-dimensional velocity obstacle region. If the relative velocity falls within this region, a potential conflict relationship exists, forming a potential conflict edge; otherwise, no potential conflict relationship exists. The modeling process is as follows.

The ellipsoid equation is given by

$$\frac{(X-x_B)^2}{d_v^2}+\frac{(Y-y_B)^2}{d_v^2}+\frac{(Z-z_B)^2}{d_l^2}=1 \quad (2)$$

Let the direction vector of the relative velocity be (v_x, v_y, v_z). Then the parametric equation of the line representing the relative velocity is given by

$$\frac{X-x_A}{v_x}=\frac{Y-y_A}{v_y}=\frac{Z-z_A}{v_z}=m \quad (3)$$

By combining these equations, we obtain the discriminant Δ. A potential conflict relationship between the aircraft exists if the following two conditions are simultaneously satisfied: (1) $\Delta>0$, indicating that the line intersects the surface at two points; (2) $\cos\alpha>0, 0^\circ<\alpha<90^\circ$, where α is the angle between the relative velocity and line segment AB.

1.3 Safety situation assessment feature matrix

Aircraft operations in the terminal area are characterized by complex procedures and highly dynamic maneuvering states. To comprehensively assess the safety situation of aircraft operations and identify potential risks, this study constructs safety situation assessment feature matrix from three perspectives: basic traffic flow parameters, aircraft maneuverability metrics, and aircraft potential conflict situation network attributes.

1.3.1 Basic traffic flow parameters

The basic traffic flow parameters include flight flow, average horizontal speed, average vertical speed, average horizontal speed ratio, and average vertical speed ratio.

(1) Flight flow, denoted as Q_t, is defined as the number of aircraft executing flight tasks, either in the departure climb or in the approach descent phase within a unit time slice in airspace.

$$Q_t = \text{count}\{\text{Flight}\}_t \quad (4)$$

where $\{\text{Flight}\}_t$ represents the set of aircraft executing flight tasks, either in the departure climb or in the approach descent phase in airspace at time t.

(2) Average horizontal speed, denoted as $\overline{V_t^h}$, is defined as the average horizontal flight speed of aircraft within a unit time slice in airspace.

$$\overline{V_t^h}=\sum_{i=1}^{Q_t} V_t^{hi}/Q_t \quad (5)$$

where V_t^{hi} represents the horizontal flight speed of aircraft i in airspace at time t.

(3) Average vertical speed, denoted as $\overline{V_t^v}$, is defined as the average vertical flight speed of aircraft within a unit time slice in airspace.

$$\overline{V_t^v}=\sum_{i=1}^{Q_t} V_t^{vi}/Q_t \quad (6)$$

where V_t^{vi} represents the vertical flight speed of aircraft i in airspace at time t.

(4) Average horizontal speed ratio, denoted as $R\,\overline{V_t^h}$, is defined as the ratio of average horizontal flight speed to the maximum horizontal flight speed of all aircraft within a unit time slice in airspace. It describes the deviation of average horizontal speed of the flight flow from the maximum value, reflecting the relative speed state in the horizontal direction.

$$R\,\overline{V_t^h}=\overline{V_t^h}/\max\_V_t^h \quad (7)$$

where $\max\_V_t^h$ represents the maximum horizontal flight speed of all aircraft in airspace at time t.

(5) Average vertical speed ratio, denoted as $R\,\overline{V_t^v}$, is defined as the ratio of average vertical flight speed to the maximum vertical flight speed of all aircraft within a unit time slice in airspace, reflecting the relative speed state in vertical direction.

$$R\,\overline{V_t^v}=\overline{V_t^v}/\max\_V_t^v \quad (8)$$

where $\max\_V_t^v$ represents the maximum vertical flight speed of all aircraft in airspace at time t.

1.3.2 Aircraft maneuverability metrics

Aircraft maneuverability metrics include average horizontal speed change, average altitude change, average vertical speed change, average heading change, horizontal speed change exceedance, altitude change exceedance, vertical speed change exceedance, and heading change exceedance.

(1) Average horizontal speed change, denoted as $\overline{\Delta V_t^{\mathrm{h}}}$, is defined as the average change in horizontal flight speed of aircraft within a unit time slice in airspace.

$$\overline{\Delta V_t^{\mathrm{h}}}=\sum_{i=1}^{Q_t}\Delta V_t^{\mathrm{h}i}/Q_t \tag{9}$$

where $\Delta V_t^{\mathrm{h}i}$ represents horizontal speed change of aircraft i in airspace at time t.

(2) Average altitude change, denoted as $\overline{\Delta A_t}$, is defined as the average change in altitude of aircraft within a unit time slice in airspace.

$$\overline{\Delta A_t}=\sum_{i=1}^{Q_t}\Delta A_t^i/Q_t \tag{10}$$

where ΔA_t^i represents the altitude change of aircraft i in airspace at time t.

(3) Average vertical speed change, denoted as $\overline{\Delta V_t^{\mathrm{v}}}$, is defined as average change in vertical flight speed of aircraft within a unit time slice in airspace.

$$\overline{\Delta V_t^{\mathrm{v}}}=\sum_{i=1}^{Q_t}\Delta V_t^{\mathrm{v}i}/Q_t \tag{11}$$

where $\Delta V_t^{\mathrm{v}i}$ represents the vertical speed change of aircraft i in the airspace at time t.

(4) Average heading change, denoted as $\overline{\Delta H_t}$, is defined as average change in heading of aircraft within a unit time slice in airspace.

$$\overline{\Delta H_t}=\sum_{i=1}^{Q_t}\Delta H_t^i/Q_t \tag{12}$$

where ΔH_t^i represents the heading change of aircraft i in airspace at time t.

(5) Horizontal speed change exceedance, denoted as Cos_t, is defined as the number of aircraft within a unit time slice in airspace whose horizontal speed change exceeds the threshold.

$$\mathrm{Cos}_t=\sum_{i=1}^{Q_t}a_t^i\quad a_t^i=\begin{cases}1 & \Delta V_t^{\mathrm{h}i}>\mathrm{limit\_}\Delta V^{\mathrm{h}}\\ 0 & \Delta V_t^{\mathrm{h}i}\leqslant\mathrm{limit\_}\Delta V^{\mathrm{h}}\end{cases} \tag{13}$$

where a_t^i represents the state variable of horizontal speed change for aircraft i in airspace at time t and limit_ΔV^{h} the threshold for horizontal speed change.

(6) Altitude change exceedance, denoted as Coa_t, is defined as the number of aircraft within a unit time slice in airspace whose altitude change exceeds the threshold.

$$\mathrm{Coa}_t=\sum_{i=1}^{Q_t}b_t^i\quad b_t^i=\begin{cases}1 & \Delta A_t^i>\mathrm{limit\_}\Delta A\\ 0 & \Delta A_t^i\leqslant\mathrm{limit\_}\Delta A\end{cases} \tag{14}$$

where b_t^i represents the state variable of the altitude change for aircraft i in airspace at time t and limit_ΔA the threshold for altitude change.

(7) Vertical speed change exceedance, denoted as Cov_t, is defined as the number of aircraft within a unit time slice in airspace whose vertical speed change exceeds the threshold.

$$\mathrm{Cov}_t=\sum_{i=1}^{Q_t}c_t^i\quad c_t^i=\begin{cases}1 & \Delta V_t^{\mathrm{v}i}>\mathrm{limit\_}\Delta V^{\mathrm{v}}\\ 0 & \Delta V_t^{\mathrm{v}i}\leqslant\mathrm{limit\_}\Delta V^{\mathrm{v}}\end{cases} \tag{15}$$

where c_t^i represents the state variable of vertical speed change for aircraft i in airspace at time t and limit_ΔV^{v} the threshold for vertical speed change.

(8) Heading change exceedance, denoted as Coh_t, is defined as the number of aircraft within a unit time slice in the airspace whose heading change exceeds the threshold.

$$\mathrm{Coh}_t=\sum_{i=1}^{Q_t}d_t^i\quad d_t^i=\begin{cases}1 & \Delta H_t^i>\mathrm{limit\_}\Delta H\\ 0 & \Delta H_t^i\leqslant\mathrm{limit\_}\Delta H\end{cases} \tag{16}$$

where d_t^i represents the state variable of the heading change for aircraft i in airspace at time t and limit_ΔH the threshold for heading change.

1.3.3 Potential conflict situation network attributes

The aircraft potential conflict situation network attributes include potential conflict quantity, potential conflict rate, number of aircraft clusters, number of aircraft in the largest cluster, network density, and average clustering coefficient.

(1) Potential conflict quantity, denoted as Cq_t, is defined as the number of aircraft with potential conflict relationships within a unit time slice in the airspace.

$$\mathrm{Cq}_t=\mathrm{count}\{\mathrm{Flight\_in\_conflict}\}_t \tag{17}$$

where $\{\mathrm{Flight\_in\_conflict}\}_t$ represents the set of aircraft with potential conflict relationships in the airspace at time t.

(2) Potential conflict rate, denoted as Cr_t, is

defined as the ratio of the number of aircraft with potential conflict relationships to the flight flow within a unit time slice in the airspace.

$$\mathrm{Cr}_t = \mathrm{Cq}_t / Q_t \tag{18}$$

(3) Number of aircraft clusters, denoted as Cc_t, is defined as the number of connected components in the aircraft potential conflict situation network within a unit time slice.

(4)Number of aircraft in the largest cluster, denoted as Cmc_t, is defined as the number of aircraft in the largest connected component of the aircraft potential conflict situation network within a unit time slice.

(5) Network density, denoted as Nd_t, is defined as the degree of connectivity in the aircraft potential conflict situation network within a unit time slice.

$$\mathrm{Nd}_t = 2v_t / e_t(e_t - 1) \tag{19}$$

where v_t denotes the number of edges and e_t the number of nodes in the network at time t.

(6) Average clustering coefficient, denoted as Acc_t, is defined as the average clustering coefficient of all target nodes in the aircraft potential conflict situation network within a unit time slice.

$$\mathrm{Acc}_t = \frac{1}{n}\sum_{i=1}^{Q_t} C_t^i \tag{20}$$

where C_t^i denotes the clustering coefficient of node i at time t.

1.4 Safety situation levels recognition model

The deep clustering algorithm can improve the performance of clustering on high-dimensional data[25]. To address the issues of dimensionality confusion and inconsistent tasks raised earlier, and to enhance clustering performance and model interpretability, this paper proposes a deep clustering network model incorporating a safety situation information capture layer, specifically designed for the field of air traffic aircraft operation safety situation recognition. This addition ensures that the encoded features effectively capture discriminative information regarding safety situations. The model comprises three modules: an autoencoder, a clustering layer, and a risk capture layer. It incorporates reconstruction loss, clustering loss, and classification loss (risk information capture loss), as depicted in Fig.6. By jointly training these three loss functions, the model simultaneously considers data reconstruction ability, clustering performance, and the capability to capture risk information from encoded features. Through the backpropagation, the parameters are optimized to ensure that the three layers are interconnected and integrated to achieve balanced optimization.

This approach, as illustrated in the following equation, helps the model learn more representative and generalizable feature representations, thereby improving the performance and effectiveness of the deep clustering model in practical applications. In

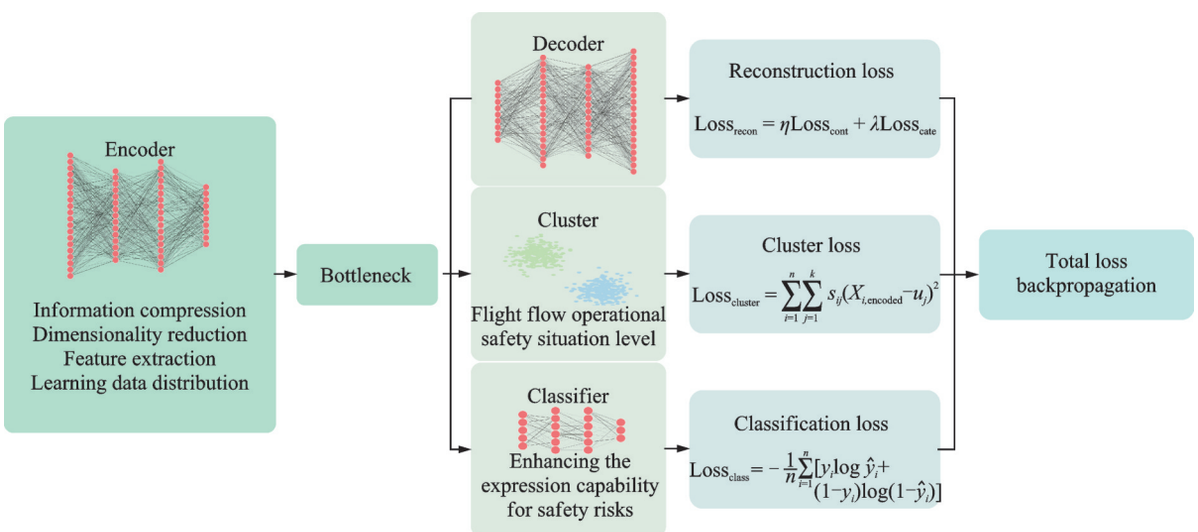

Fig.6 Flow chart of risk-aware deep clustering model

the recognition module, the aircraft operational safety situation feature matrix $\boldsymbol{X}\in\mathbf{R}^{S\times F\times N}$ is reconstructed to $\boldsymbol{X}\in\mathbf{R}^{(S\cdot N)\times F}$ to conform to the model input.

$$\mathrm{Loss}_{\mathrm{total}}=\partial\mathrm{Loss}_{\mathrm{recon}}+\beta\mathrm{Loss}_{\mathrm{class}}+\gamma\mathrm{Loss}_{\mathrm{cluster}} \tag{21}$$

where $\mathrm{Loss}_{\mathrm{total}}$ represents the total loss, $\mathrm{Loss}_{\mathrm{recon}}$ the reconstruction loss, $\mathrm{Loss}_{\mathrm{class}}$ the classification loss, and $\mathrm{Loss}_{\mathrm{cluster}}$ the clustering loss. The coefficients ∂, β and γ correspond to the weights assigned to different losses.

1.4.1 Autoencoder

An autoencoder is an unsupervised learning neural network consisting of an encoder and a decoder. It effectively captures complex and nonlinear patterns in the data by learning and reconstructing the input data[26]. This allows the autoencoder to provide richer and more discriminative feature representations for safety situational awareness clustering.

The encoder is responsible for transforming the input data into latent codes to capture the underlying representations of the data. Its forward propagation process can be described by

$$\boldsymbol{X}_{\mathrm{encoded}}=\mathrm{Encoder}(\boldsymbol{X})=\mathrm{ReLU}(\mathrm{Linear}(\boldsymbol{X})+\mathrm{Dropout}(\mathrm{Linear}(\boldsymbol{X}))) \tag{22}$$

where $\boldsymbol{X}_{\mathrm{encoded}}$ represents the encoded features, $\boldsymbol{X}$ the original features, ReLU the activation function, Linear the fully connected layer, and Dropout the dropout layer used to prevent overfitting.

The decoder receives the output from the encoder and restores it to the original input data through a series of transformations. Its goal is to reconstruct the original input data as accurately as possible to maintain consistency with the original data. The forward propagation process can be described by

$$\boldsymbol{X}_{\mathrm{recon}}=\mathrm{Decoder}(\boldsymbol{X}_{\mathrm{encoded}})=\mathrm{ReLU}(\mathrm{Linear}(\boldsymbol{X}_{\mathrm{encoded}})+\mathrm{Dropout}(\mathrm{Linear}(\boldsymbol{X}_{\mathrm{encoded}}))) \tag{23}$$

where $\boldsymbol{X}_{\mathrm{recon}}$ represents the reconstructed features.

The feature matrix often includes both continuous and discrete features. The mean squared error loss function is used for continuous features, while the cross-entropy loss function is employed for discrete features, as described by

$$\mathrm{Loss}_{\mathrm{cont}}=\frac{1}{n}\sum_{i=1}^{n}(X_i^{\mathrm{cont}}-X_{i,\mathrm{recon}}^{\mathrm{cont}})^2 \tag{24}$$

$$\mathrm{Loss}_{\mathrm{cate}}^{\mathrm{b}}=-\frac{1}{n}\sum_{i=1}^{n}[X_i^{\mathrm{b,cate}}\log X_{i,\mathrm{recon}}^{\mathrm{b,cate}}+(1-X_i^{\mathrm{b,cate}})\log(1-X_{i,\mathrm{recon}}^{\mathrm{b,cate}})] \tag{25}$$

$$\mathrm{Loss}_{\mathrm{cate}}^{\mathrm{m}}=-\frac{1}{n}\sum_{i=1}^{n}\sum_{c=1}^{C}X_{i,c}^{\mathrm{m,cate}}\log X_{i,\mathrm{recon}}^{\mathrm{m,cate}} \tag{26}$$

$$\mathrm{Loss}_{\mathrm{cate}}=\mathrm{Loss}_{\mathrm{cate}}^{m}+\mathrm{Loss}_{\mathrm{cate}}^{b} \tag{27}$$

$$\mathrm{Loss}_{\mathrm{recon}}=\eta\mathrm{Loss}_{\mathrm{cont}}+\lambda\mathrm{Loss}_{\mathrm{cate}} \tag{28}$$

where n is the number of samples, $\mathrm{Loss}_{\mathrm{cont}}$ the loss for continuous features, $\mathrm{Loss}_{\mathrm{cate}}$ the loss for discrete features, $\mathrm{Loss}_{\mathrm{cate}}^{\mathrm{b}}$ the loss for binary discrete features, $\mathrm{Loss}_{\mathrm{cate}}^{\mathrm{m}}$ the loss for multi-class discrete features, X_i^{cont} the original continuous features, $X_{i,\mathrm{recon}}^{\mathrm{cont}}$ the reconstructed continuous features, $X_i^{\mathrm{b,cate}}$ true label for the original binary discrete features, $X_{i,\mathrm{recon}}^{\mathrm{b,cate}}$ the predicted probability for the reconstructed binary discrete features, C the total number of classes, $X_{i,c}^{\mathrm{m,cate}}$ the true label for the original multi-class discrete features, and $X_{i,\mathrm{recon}}^{\mathrm{m,cate}}$ the predicted probability for the reconstructed multi-class discrete features. The coefficients η and λ correspond to the weights assigned to different losses.

1.4.2 Clustering layer

The K-means algorithm is a commonly used unsupervised learning algorithm for partitioning a dataset into K distinct clusters. This method is simple, efficient, and easy to interpret and understand, exhibiting good scalability for large-scale datasets. Therefore, in this paper, the K-means algorithm is employed at the clustering layer, using the encoded features as the input for this layer. The minimized objective function, used as the loss function for the clustering layer, is given by

$$\mathrm{Loss}_{\mathrm{cluster}}=\sum_{i=1}^{n}\sum_{j=1}^{k}s_{ij}(X_{i,\mathrm{encoded}}-u_j)^2 \tag{29}$$

where s_{ij} indicates whether sample i belongs to cluster j, and u_j the jth cluster center.

1.4.3 Safety risk information capture layer

To ensure that the encoded features retain sufficient capability to express safety situational awareness, this paper introduces a safety risk capture layer. This layer is a supervised learning layer designed to use encoded features to distinguish whether active aircraft are in potential conflict. The higher the

classification accuracy, the stronger the risk capture capability of the encoded features. The cross-entropy loss function is used as the loss function for this layer, as shown in Eq.(30). By incorporating the supervised learning layer, the specific contributions of the encoded features to the operational safety situational awareness of aircraft can be more easily interpreted.

$$\text{Loss}_{\text{class}} = -\frac{1}{n}\sum_{i=1}^{n}\left[y_i \log \widehat{y}_i + (1-y_i)\log\left(1-\widehat{y}_i\right)\right] \tag{30}$$

where y_i represents true labels, and $\widehat{y}_i$ the predicted probabilities that the sample is classified as positive.

1.5 Safety situation levels prediction model

The terminal area connects with cruising flights above and with takeoff and landing operations below, forming a complex interwoven region that integrates the airport surface and the route network. This area is characterized by high aircraft maneuverability and traffic density. In the field of air traffic safety situational awareness prediction, to fully consider the spatiotemporal heterogeneity of situational evolution within the terminal area, this paper proposes an attention based spatial-temporal graph convolutional network model that accounts for spatiotemporal coupling changes. The situational levels are used as new features, and a time window of T moments is adopted, sliding by one moment at a time, to divide the dataset. The dataset $\boldsymbol{X}\in\mathbf{R}^{S\times F\times N}$ is reshaped to $\boldsymbol{X}\in\mathbf{R}^{S'\times N\times F\times T}$, where S' represents the new number of samples. This model primarily consists of two modules: the attention mechanism and the convolutional module. Some parts of the modules involve dimension order adjustments, which are provided in the code. The framework is shown in Fig.7.

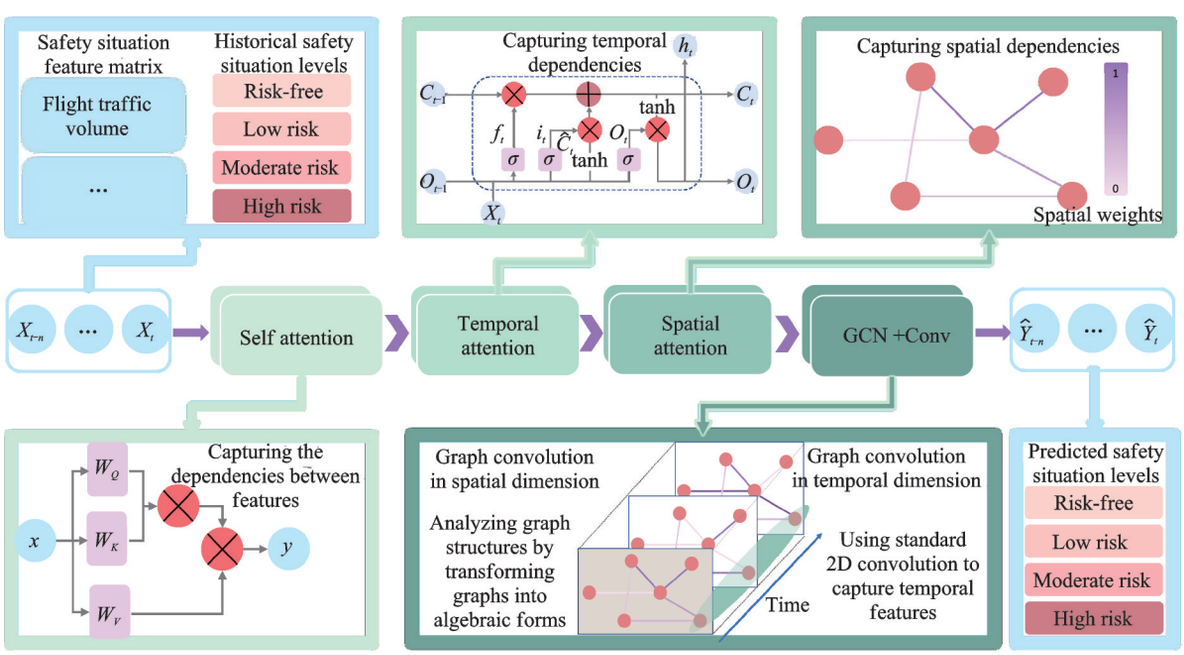

Fig.7 Attention based spatial-temporal graph convolutional networks

1.5.1 Attention mechanism

The attention mechanism refers to a technique in neural networks that simulates the human attention focusing behavior, allowing the model to automatically decide which part of the information to focus on when processing large-scale input data. This enhances the efficiency of data processing and improves the model's performance. This paper integrates self-attention mechanisms, temporal attention mechanisms, and spatial attention mechanisms into the model to capture the complex relationships between features and the spatiotemporal heterogeneity of the data, thereby improving the model's performance in analyzing spatiotemporal data tasks.

(1)Self-attention mechanism

The self-attention mechanism originates from

Input: Safety situation feature matrix and levels $\boldsymbol{X}$ and adjacency matrix $\boldsymbol{A}$
Data Processing
Model Initialization
Model Training:
For each training epoch
For each mini-batch:
For each node and time step in the batch:
Pass $\boldsymbol{X}$ through the self-attention mechanism layer (Eqs.(31—32)) to obtain $\boldsymbol{X}_{\text{self}}$
Pass $\boldsymbol{X}_{\text{self}}$ through the temporal attention mechanism layer (Eqs.(33—34)) to obtain $\boldsymbol{X}_{\text{Temp}}$
Pass $\boldsymbol{X}_{\text{Temp}}$ through the spatial attention mechanism layer (Eqs.(35—36)) to obtain $\boldsymbol{S}$
Pass $\boldsymbol{X}$, $\boldsymbol{S}$ and $\boldsymbol{A}$ through the spatial convolution layer (Eqs.(37—41)) to obtain $\boldsymbol{X}_{\text{cheb}}$
Pass $\boldsymbol{X}_{\text{cheb}}$ through the temporal convolution layer (Eq.(42)) to obtain $\boldsymbol{X}_{\text{time}}$
pass $\boldsymbol{X}$, $\boldsymbol{X}_{\text{cheb}}$ through the residual layer (Eq.(43)) to obtain $\boldsymbol{X}_{\text{res}}$
Pass $\boldsymbol{X}_{\text{res}}$ through the classification layer (Eq.(44)) to obtain the final output Y
Compute the total loss, perform backpropagation, and update model parameters.
Save the model parameters for the current epoch
Output: Select the model with the best performance on the validation set as the final ASTGCN model

the Transformer model proposed in the paper "Attention is All You Need" by Google team[27], which initiated a new paradigm in the field of deep learning. The self-attention mechanism allows the model to dynamically adjust its focus among different positions within a single sequence, assessing the interrelationships and importance of various features. This helps the model identify the features most crucial for prediction. This paper uses the scaled dot-product attention mechanism to extract the weights among features. The calculation steps are as follows, where the input is $\boldsymbol{X}\in\mathbf{R}^{S'\times N\times F\times T}$ and the output $\boldsymbol{X}_{\text{self}}\in\mathbf{R}^{S'\times N\times F\times T}$.

Step 1 Compute $\boldsymbol{Q}$ (Query), $\boldsymbol{K}$ (Key), and $\boldsymbol{V}$ (Value);

Step 2 Calculate the attention scores matrix using $\boldsymbol{Q}$, $\boldsymbol{K}$ and $\boldsymbol{V}$ by

$$\boldsymbol{A}=\frac{\boldsymbol{Q}\cdot\boldsymbol{K}^{\mathrm{T}}}{\sqrt{F_{\text{in}}}} \tag{31}$$

where F_{in} is the dimension of features.

Step 3 Output the self-attention weighted matrix by

$$\boldsymbol{X}_{\text{self}}=\text{soft max}(\boldsymbol{A})\boldsymbol{V}\in\mathbf{R}^{S'\times N\times F\times T} \tag{32}$$

(2)Temporal attention mechanism

As a special type of recurrent neural network (RNN), LSTM can capture long-term dependencies in time series data through its unique internal structure, Therefore, this paper uses the LSTM layer to capture the long-term dependencies and temporal dynamics in the time series data. Then, a fully connected layer is used to map the hidden states output by the LSTM layer at each time step (which contain temporal dynamic information) into a new feature space. The attention weights for each time step relative to other time steps are generated using a softmax function, ultimately producing a time attention-weighted matrix. The input is $\boldsymbol{X}_{\text{self}}\in\mathbf{R}^{S'\times N\times F\times T}$, reshaped to $\boldsymbol{X}_{\text{self}}\in\mathbf{R}^{(S'\cdot N)\times T\times F}$. $\boldsymbol{x}_t=\boldsymbol{X}_{\text{self}}[:,t,:]$, $t\in\{1,2,\cdots,T\}$ is the input at the current time step t. The output is $\boldsymbol{X}_{\text{Temp}}\in\mathbf{R}^{S'\times N\times F\times T}$.

Step 1 Output time weights through the LSTM model

$$\boldsymbol{T}_{\text{w}}=\text{soft max}(\boldsymbol{W}_m\cdot h_t+b_m)\in\mathbf{R}^{S'\times N\times T\times T} \tag{33}$$

where $\boldsymbol{T}_{\text{w}}$ is the time weight matrix, $\boldsymbol{W}_m$ the weight matrix for the fully connected layer, $\boldsymbol{h}_t$ the hidden state and $\boldsymbol{b}_m$ the bias term for the fully connected layer.

Step 2 Output time attention weighted matrix by

$$\boldsymbol{X}_{\text{Temp}}=\boldsymbol{X}_{\text{self}}\cdot\boldsymbol{T}_{\text{w}}\in\mathbf{R}^{S'\times N\times F\times T} \tag{34}$$

(3)Spatial attention mechanism

This paper employs a spatial attention mechanism to adaptively capture the spatial correlations of safety situational awareness between nodes in the airspace network through multiple learnable parameters and matrix operations. The input is $\boldsymbol{X}_{\text{Temp}}\in\mathbf{R}^{S'\times N\times F\times T}$ and the output is $\boldsymbol{S}\in\mathbf{R}^{S'\times N\times N}$. The spatial attention weight matrix is computed as

$$\boldsymbol{S}=P_s\cdot\sigma\left((\boldsymbol{X}_{\text{Temp}}W_1)W_2(W_3\boldsymbol{X}_{\text{Temp}})^{\mathrm{T}}+\boldsymbol{b}_s\right) \tag{35}$$

$$\boldsymbol{S}_{\text{w}}=\text{soft max}(\boldsymbol{S}) \tag{36}$$

where P_s, W_1, W_2 and W_3 are learnable parameters.

1.5.2 Graph convolution

(1)Graph convolution in spatial dimension

The terminal area airspace network is a typical non-Euclidean data structure. Therefore, this paper uses a spectral graph convolutional neural network (GCN)[28] to explore the spatial dynamic relationships of air traffic safety situational awareness in the terminal area. In spectral GCN, the convolution operation is performed in the spectral domain of the graph (i.e., the domain of the graph's eigenvalues and eigenvectors). This utilizes the eigen decomposition of the graph Laplacian matrix, combining features of nodes with characteristics of the graph for convolution operations. The specific steps are as follows, where the input is $\boldsymbol{X}\in\mathbf{R}^{S'\times N\times F\times T}$ and $\boldsymbol{S}\in\mathbf{R}^{S'\times N\times N}$, and the output is $\boldsymbol{X}_{\text{cheb}}\in\mathbf{R}^{S'\times N\times F_{\text{spcace}}\times T}$.

Step 1 Spectral representation of graph signals

In graph theory, each graph can be represented by a corresponding symmetric normalized Laplacian matrix, denoted as $L=I_n-D^{-\frac{1}{2}}AD^{-\frac{1}{2}}$, where D represents the degree matrix, A the adjacency matrix, and I_n the identity matrix of order n. The eigen decomposition of L yields $L=U\Lambda U^{-1}=U\Lambda U^{\mathrm{T}}$, where Λ is a diagonal matrix of eigenvalues, and U the matrix of eigenvectors (Fourier basis). The Fourier transform of the graph signal $\boldsymbol{x}_t=\boldsymbol{X}[:,:,:,t]$, $t\in\{1,2,\cdots,T\}$ at time t is $\hat{\boldsymbol{x}}_t=\boldsymbol{U}^{\mathrm{T}}\boldsymbol{x}_t$ and the inverse transform $\boldsymbol{x}_t=\boldsymbol{U}\hat{\boldsymbol{x}}_t$.

Step 2 Graph convolution operation

Graph convolution is performed by using a diagonalized linear operator defined in the Fourier domain to equivalently replace the classical convolution operator[29]. The convolution operation on graph G^s with a filter g_θ is given by

$$g_\theta *_{G^s}\boldsymbol{x}_t=g_\theta(L)\boldsymbol{x}_t=g_\theta(\boldsymbol{U}\Lambda\boldsymbol{U}^{\mathrm{T}})\boldsymbol{x}_t=\boldsymbol{U}g_\theta(\Lambda)\boldsymbol{U}^{\mathrm{T}}\boldsymbol{x}_t \tag{37}$$

where "$*_{G^s}$"denotes a graph convolution operation.

To reduce computational costs, the convolution filter is approximated using Chebyshev polynomials. The Chebyshev recursive expression is given by

$$T_k(x)=2xT_{k-1}(x)-T_{k-2}(x) \tag{38}$$

where $T_0(x)=1$ and $T_1(x)=x$. Therefore, the graph convolution operation can be expressed as

$$g_\theta *_{G^s}\boldsymbol{x}_t=g_\theta(L)\boldsymbol{x}_t\approx\sum_{k=0}^{K-1}\theta_kT_k(\tilde{L})\boldsymbol{x}_t \tag{39}$$

$$\tilde{L}=(2/\lambda_{\max})L-I_n \tag{40}$$

where θ_k is the Chebyshev polynomial coefficient, and $\lambda_{\max}$ the largest eigenvalue of the Laplacian matrix.

Adding spatial attention weights gives

$$g_\theta *_{G^s}\boldsymbol{x}_t=g_\theta(L)\boldsymbol{x}_t\approx\sum_{k=0}^{K-1}\theta_k\left(\boldsymbol{S}_{\text{w}}\odot T_k(\tilde{L})\right)\boldsymbol{x}_t=\boldsymbol{y}_t \tag{41}$$

where "$\odot$" represents the Hadamard product. Integrating outputs across all time steps yields $\boldsymbol{X}_{\text{cheb}}=(\boldsymbol{y}_1,\boldsymbol{y}_2,\cdots,\boldsymbol{y}_T)\in\mathbf{R}^{S'\times N\times F_{\text{space}}\times T}$, where F_{space} denotes the number of spatial convolution filters.

(2)Graph convolution in temporal dimension

To further extract the dynamic changes and dependencies of the features processed by the graph convolution layer in the temporal dimension, this paper uses 2D convolution to incorporate information from adjacent time steps, forming richer and more expressive temporal feature representations. The input is $\boldsymbol{X}_{\text{cheb}}\in\mathbf{R}^{S'\times N\times F_{\text{spcae}}\times T}$ and the output is $\boldsymbol{X}_{\text{time}}\in\mathbf{R}^{S'\times N\times F_{\text{time}}\times T}$, where F_{time} denotes the number of temporal convolution filters.

$$\boldsymbol{X}_{\text{time}}=\text{Time\_conv2d}(\boldsymbol{X}_{\text{cheb}}) \tag{42}$$

1.5.3 Residual connection and layer normalization

Residual connections are introduced to address issues such as overfitting, gradient vanishing, and gradient explosion caused by network depth. 2D convolution is used to adjust feature dimensions, and layer normalization is applied to stabilize the training process and accelerate convergence. A Dropout layer is also added to prevent model overfitting. The input is $\boldsymbol{X}\in\mathbf{R}^{S'\times N\times F\times T}$ and $\boldsymbol{X}_{\text{time}}\in\mathbf{R}^{S'\times N\times F_{\text{time}}\times T}$, and the output is $\boldsymbol{X}_{\text{res}}\in\mathbf{R}^{S'\times N\times F_{\text{time}}\times T}$.

$$\boldsymbol{X}_{\text{res}}=\text{Dropout}\Big(\text{Layernorm}(\text{ReLU}(\boldsymbol{X}_{\text{time}}+\text{Res\_conv2d}(\boldsymbol{X})))\Big) \tag{43}$$

1.5.4 Final convolution and classifier layer

The final convolution refines and transforms the features processed by the main modules, aggregating information learned across different feature channels to achieve the final situational level classification task. The input is $\boldsymbol{X}_{\text{res}} \in \mathbf{R}^{S' \times N \times F_{time} \times T}$, and the output is $\boldsymbol{Y} \in \mathbf{R}^{S' \times N \times C \times T'}$, where T' denotes the number of future time steps to be predicted, and C the number of prediction categories.

$$\boldsymbol{Y} = \text{Classifier\_conv2d}(\text{final\_conv2d}(\boldsymbol{X}_{\text{res}})) \quad (44)$$

2 Numerical Experiment

This section will conduct various experiments based on the ADS-B data in the terminal area of Chinese civil aviation to evaluate the performance of the models and analyze the spatiotemporal coupling evolution patterns of safety situational levels.

2.1 Date description

Xi'an Terminal Area is one of the largest and busiest terminal areas in northwest China. The area features a dense distribution of both military and civilian airports, with an ever-increasing number of flights. In 2019, Xi'an Xianyang International Airport ranked the seventh nationwide in terms of passenger throughput as shown in Fig.8 (a). Therefore, this paper selects the Xi'an Terminal Area as the experimental subject.

There are five approach sectors in the Xi'an terminal area, with altitude range boundaries set at 1 800, 3 000, and 6 000 m. The flight traffic exhibits a clear north-south flow pattern. To describe the spatiotemporal characteristics of flight flows in the airspace of the terminal area, as shown in Fig.8(b), the terminal area is divided into four sub-airspaces (Airspace 1: 0—1 800 m; Airspace 2: 1 800—3 000 m, Airspace 3: south of 3 000—6 000 m; Airspace 4: north of 3 000—6 000 m). What is more, referring to the aircraft arrival and departure procedures, a sub-airspace adjacency matrix is constructed. Accordingly, ADS-B data from the four sub-airspaces, spanning from July 1, 2019, to July 7, 2019, are selected.

Given the complex airspace structure and the dynamic maneuvering of aircraft in the terminal area, rapid detection and response to potential safety issues are crucial to ensuring flight safety. Therefore, this paper constructs a time-varying potential conflict situation network at 10 s intervals to compute basic traffic flow parameters, aircraft maneuverability metrics, and aircraft potential conflict situation network attributes, thereby establishing an aircraft operational safety situational awareness feature matrix $\boldsymbol{X} \in \mathbf{R}^{60\,480 \times 19 \times 4}$ (with a total of 60 480 rows and 19 columns for a single node).

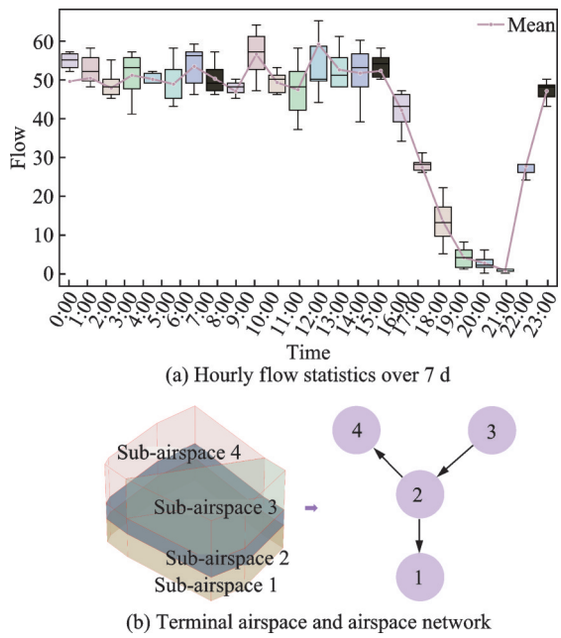

(a) Hourly flow statistics over 7 d

(b) Terminal airspace and airspace network

Fig.8 Date description

2.2 Experimental setting

This paper implements the RADCM and ASTGCN models based on the Pytorch framework. The experimental environment consists of Windows 11, Python 3.9.0, Pytorch 2.1.0, and an Intel(R) Core (TM) i5-9400F CPU @ 2.90 GHz.

In the RADCM model, the key parameter settings are shown in Table 1.

In the ASTGCN model, the key parameter settings are shown in Table 2.

2.3 Experimental results

2.3.1 Analysis of recognition model training results

Fig.9 illustrates the progressive convergence of the proposed RADCM model during the training and testing processes. The reconstruction loss, clustering loss, validation loss and classification loss all

Table 1 Parameter settings of RADCM

Parameter	Setting
Dropout rate	0.15
β	1
η	1
Number of classes	2
Hidden dim	126
∂	1
γ	0.2
λ	1
Number of clusters	3
Latent dim	18

Table 2 Parameter setting of ASTGCN

Parameter	Setting
Time steps	24
Future steps	3
Time strides	3
Number of time filters	64
Number of Chebyshev filters	64
Order of Chebyshev polynomial	2
Hidden dim	65
Dropout rate	0.3
Batch size	128
Learning rate	0.001
Learning rate decay	0.95
Number of ASTGCN blocks	2

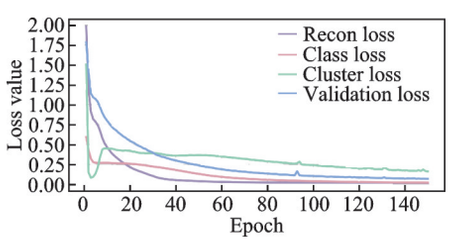

Fig.9 Training and testing of the RADCM model

exhibit a continuous downward trend. The reduction in reconstruction loss indicates that the model performs well in retaining the original data features. The decrease in clustering loss reflects the model's increasingly clear clustering effect in the feature space. The decline in classification loss ensures that the encoded features possess a certain risk-capturing capability, demonstrating the model's effectiveness in safety situation recognition. The continuous decrease in validation loss indicates that the model has good generalization ability.

The clustering effect is visualized using principal component analysis (PCA), whose results are shown in Fig.10. With the progression of the model training, different categories of data gradually separate on the two-dimensional plane, displaying more distinct clustering boundaries.

Additionally, as shown in Fig.11, during the first 40 epochs, although the model's silhouette coefficient is relatively high, the classification loss remains high and has not yet converged. This indicates that the encoded features do not effectively capture the discriminative information of the safety situation. If the encoded features are clustered at this stage, good clustering performance might be achieved, but it will lead to a mismatch between the dimensionality-reduced features and the clustering objectives.

Table 3 presents the clustering performance of the proposed RADCM model compared to baseline clustering models in the task of safety situation level recognition. The trained model is used to classify the safety situation levels of the entire dataset. The study finds that the RADCM model outperforms traditional clustering methods in terms of the Silhouette Coefficient, Calinski-Harabasz Index, and Davies-Bouldin Index.

This indicates that deep clustering can more effectively partition the dataset, generating clusters with greater distinguishability.

Table 4 presents the clustering performance of the proposed RADCM model compared to the baseline models that cluster after dimensionality reduction in the task of safety situation level recognition. The RADCM model still demonstrates superior performance.

Although clustering the features after dimensionality reduction improves clustering performance relative to traditional clustering models, this approach severs the relationship between feature reduction and the situation recognition task. Consequently, it is challenging to determine whether the reduced features effectively capture the discriminative information of the safety situations.

In summary, the RADCM model has powerful feature extraction capabilities, enabling it to capture more complex patterns and structures within the da-

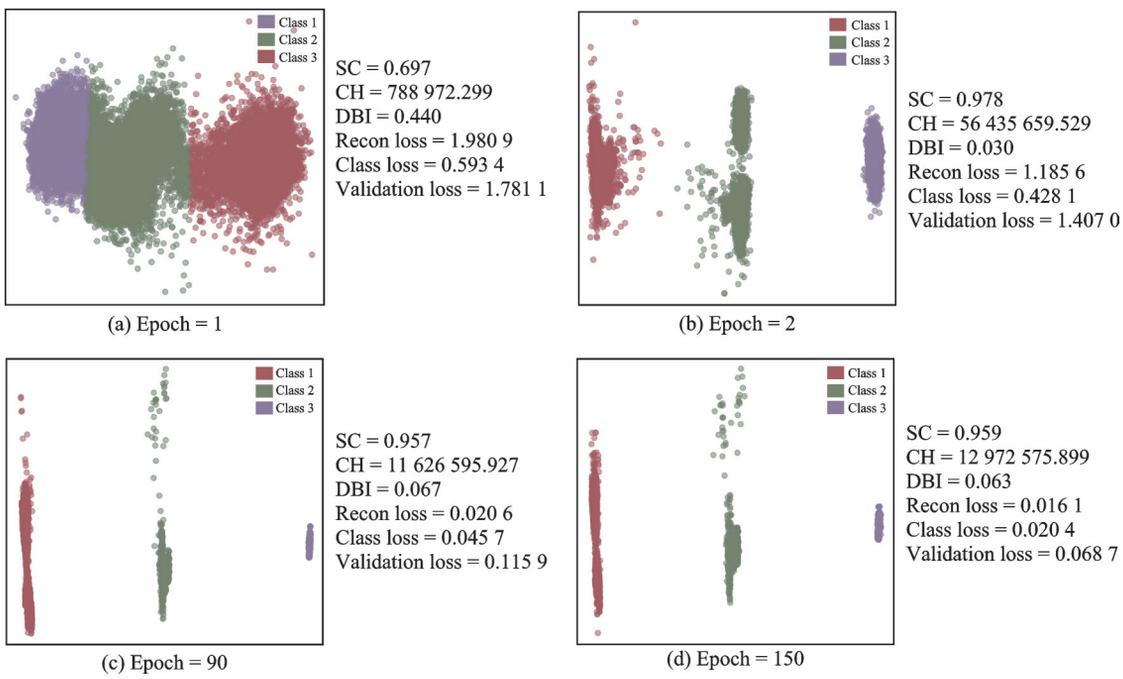

Fig.10 Cluster visualization

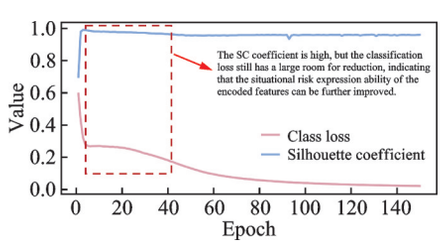

Fig.11 Class loss and SC per epoch

Table 3 Comparison of clustering models

Evaluation metrics	RADCM	FCM	*K*-means
SC	0.97	0.32	0.33
CH	17 770 989.86	29 117.26	33 689.70
DBI	0.06	1.75	1.40

ta, thereby avoiding the curse of dimensionality. This makes it perform better in handling nonlinear and complex data distributions. The addition of the safety situation risk information capture layer ensures that the encoded features possess a certain ability to distinguish aircraft operational safety risks, aligning the encoded features with the situation recognition task.

By employing the RADCM model to cluster the dataset, the safety levels of historical time slices are determined. Using LightGBM to analyze feature importance as shown in Fig.12, it is evident that the key indicators include $\overline{\Delta H_t}$, Cc_t, Cr_t, Cmc_t, $\overline{\Delta A_t}$, Q_t, Cq_t and $\overline{V_t^{\mathrm{h}}}$. The mean values of these key indicators are being statistically across different safety situation levels, as shown in Table 5.

Under high-risk safety situations, the flight flow reaches its peak, accompanied by the lowest average horizontal flight speed, indicating relatively slower traffic movement. Additionally, the average heading change of traffic is significant, while altitude changes are comparatively minor, resulting in a dense and complex network of potential conflicts with high volumes and rates of potential conflicts. In such scenarios, high traffic flow and low-speed operations may prolong flight delays, exacerbating air traffic congestion, tightening airspace resources, and increasing the likelihood of potential conflicts, thereby elevating safety risks.

In contrast, under low-risk safety situations,

Table 4 Comparison of dimensionality reduction followed by clustering models

Evaluation metrics	RADCM	TSNE-FCM	TSNE-*K*-means	PCA-FCM	PCA-*K*-means
SC	0.97	0.37	0.37	0.80	0.80
CH	17 770 989.86	82 588.95	82 893.01	516 532.95	516 573.26
DBI	0.06	0.87	0.87	0.32	0.32

moderate flight flow and higher average horizontal flight speeds are observed, with no potential conflicts present, leading to an orderly and well-structured traffic flow. Medium-risk safety situations, as a transitional state between high- and low-risk situations, exhibit the lowest flight flow but not the highest average horizontal speed. With the largest average altitude changes and occasional potential conflicts, this state demonstrates operational complexity and instability. It neither matches the tension of high-risk scenarios nor maintains the clarity of low-risk ones, embodying a higher degree of uncertainty and potential hazards.

Based on the above analysis, the attributes of each safety level can be summarized as follows.

(1) Safety level 0, no risk: The number of active aircraft in the airspace does not meet the necessary conditions for forming potential conflicts.

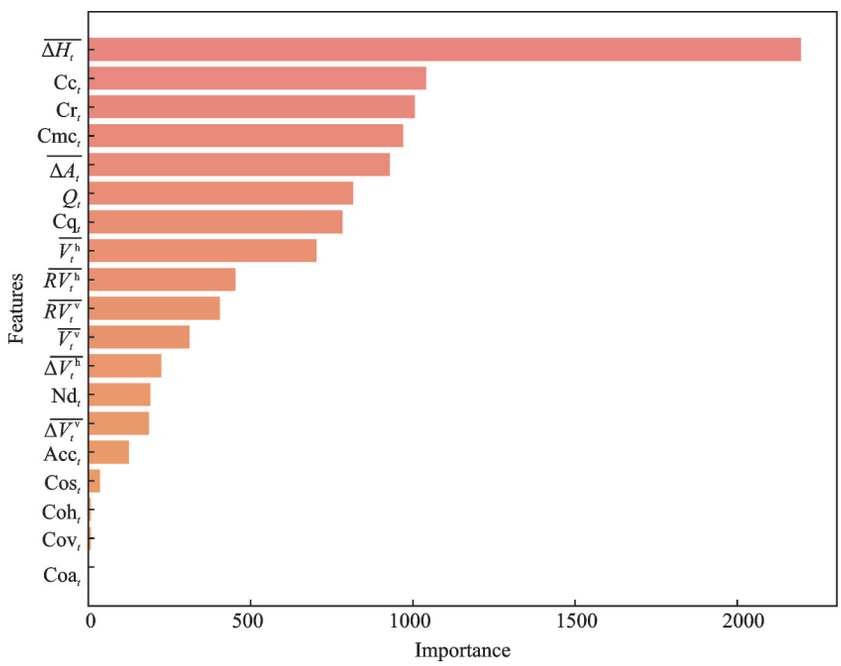

Fig.12 Feature importance

Table 5 Mean values of these key indicators

Safety level	$\overline{\Delta H_t}$	Cc_t	Cr_t	Cmc_t	$\overline{\Delta A_t}$	Q_t	Cq_t	$\overline{V_t^h}$
1	3.29	3.00	0.00	1.00	52.12	3.00	0.00	540.66
2	3.73	2.05	0.00	1.00	54.95	2.05	0.01	529.50
3	4.08	2.83	0.48	1.75	49.58	3.61	1.47	478.80

(2) Safety level 1, low risk: The number of aircraft in the airspace is moderate, meeting the necessary conditions for potential conflicts, with low traffic complexity, but no potential conflicts exist.

(3) Safety level 2, moderate risk: There are many aircraft in the airspace, with moderate traffic complexity, and a few potential conflicts. Moderate air traffic control is required to ensure that aircraft follow designated routes and altitude levels to prevent potential conflicts.

(4) Safety level 3, high risk: The airspace is densely populated with aircraft, meeting the necessary conditions for potential conflicts, with high traffic complexity, and numerous potential conflicts. Strict air traffic control is required, demanding precise adherence to control instructions, and flow control measures may need to be implemented.

2.3.2 Analysis of predication model training results

Fig.13 shows training and testing results of the ASTGCN model. Fig.13(a) depicts the convergence of the training loss. The model's loss on the training set is very low, indicating that the error between the model's predicted output and the actual

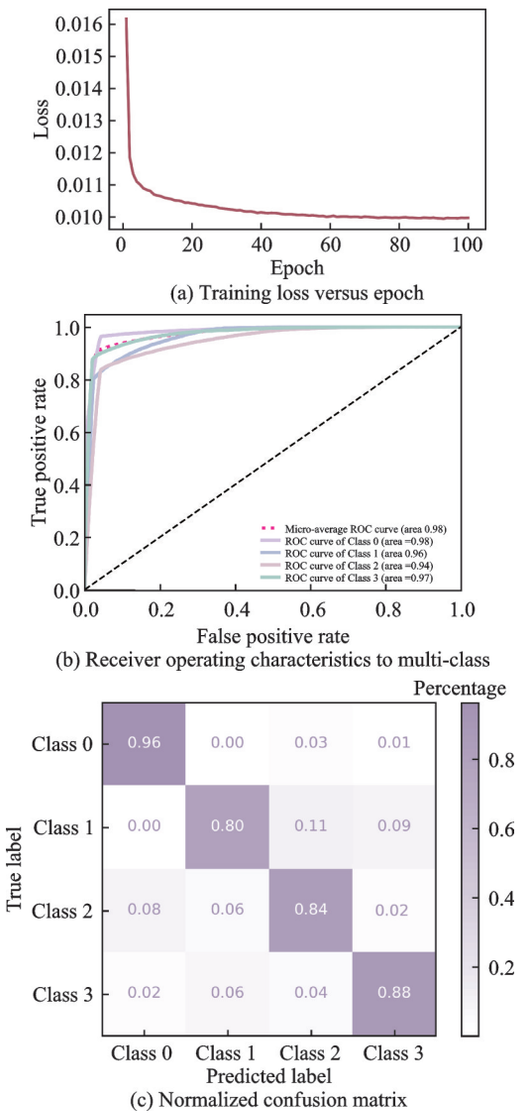

Fig.13 Training and testing results of the ASTGCN model

data is minimal. The accuracy on the training set is 0.91, with an F_1 score of 0.87. Fig.13(b) shows the ROC evaluation curve and AUC area of the ASTGCN model on the test set. In real-world applications, situation datasets may exhibit class imbalance, where the distribution of data across different situation levels is uneven. The ROC curve is robust in such scenarios, and an AUC area closer to 1 indicates better model performance. The AUC areas for Classes 0 through 3 are 0.98, 0.96, 0.94, and 0.97, respectively, with a micro-average AUC area of 0.98, demonstrating the model's strong performance. Fig.13(c) presents the normalized confusion matrix on the test set, showing that the model has high classification accuracy across all categories. In summary, the model exhibits good predictive performance on both training and test sets.

The robustness and generalization ability of the model are key to evaluating its practicality. Therefore, this paper conducts cross-testing experiments to further assess the model. The K-fold cross-testing involves dividing the dataset into K mutually exclusive subsets of similar size. Each time, one subset is used as the test set, and the remaining $K-1$ subsets are used as the training set. This process is repeated K times, each time with a different subset as the test set, to evaluate the model's stability and generalization ability.

Fig.14 shows the accuracy and F_1 score of the training and test sets across different folds. In the training set, both accuracy and F_1 score remain high and stable across all five folds (accuracy ranging from approximately 90.68% to 90.75%, and F_1 score ranging from approximately 87.02% to 87.12%), indicating consistent learning by the model on the training data. In the test set, the accuracy and F_1 score also exhibit relative stability (accuracy ranging from approximately 90.41% to 90.81%, and F_1 score ranging from approximately 86.67% to 87.24%). The maximum difference in accuracy and F_1 score between the training and test sets does not exceed 0.5%, showing that the model's performance on the training and test sets is close, indicating no significant overfitting. This demonstrates that the model has good generalization ability.

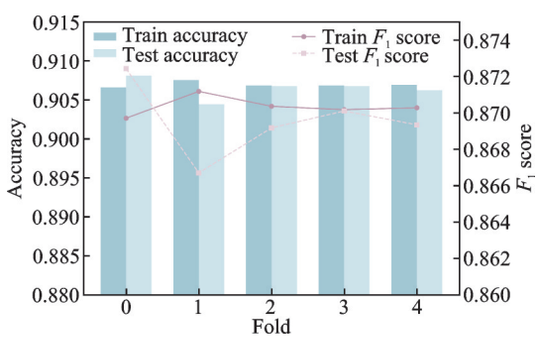

Fig.14 K-fold cross-testing results

Table 6 presents comparative experimental results between the ASTGCN model and the baseline models (TGCN, LSTM, GRU). It is evident that the ASTGCN model demonstrates superior performance across all evaluation metrics.

Table 6 Comparative experimental results

Model	Accuracy	F_1	AUC
ASTGCN	**0.91**	**0.87**	**0.98**
TGCN	0.84	0.84	0.94
LSTM-Node 1	0.82	0.81	0.92
LSTM-Node 2	0.79	0.79	0.92
LSTM-Node 3	0.79	0.79	0.93
LSTM-Node 4	0.83	0.83	0.93
GRU-Node 1	0.85	0.85	0.94
GRU-Node 2	0.81	0.81	0.93
GRU-Node 3	0.84	0.84	0.94
GRU-Node 4	0.86	0.86	0.94

2.3.3 Analysis of safety situation levels characteristics

Table 7 shows the distribution of safety levels for flight flows within 60 480 time slices across different sub-airspaces. It is noticeable that high-risk situations frequently occur in the flight flows within sub-airspace Node 1 and Node 2. This is because the civil aviation terminal area below 3 000 m is typically the final stage of convergence for approaching aircraft and the initial stage of divergence for departing aircraft, marking a critical phase of arrival and departure. In this altitude range, the flight density is high, and flights need to perform frequent altitude changes and maneuvers such as turns, making it prone to potential conflicts between aircraft, especially near flight intersection points.

(1) Hourly distribution of safety situation levels

Fig.15 shows percentage of safety levels per-hour for the first three days across different sub-airspaces. Overall, it presents a trend of transitioning from low- to high-risk situations and then gradually back to low-risk. From 18:00 to 22:00, the airspace flight flows are predominantly in a no-risk state, indicating a lower level of aircraft activity during these hours.

In Nodes 1, 2, and 3, the proportion of medium- to high-risk flight flows exceeds 50% during many time periods. In contrast, flight flows in Node 4 are predominantly characterized by no- and low-risk statuses most of the time. In the hourly distribution of safety situational levels in Node 1, multiple time points show a high-risk status exceeding 0.5, crossing the red line. In Node 2, high-risk statuses exceed 0.5 at a few time points, whereas in Nodes 3 and 4, there are virtually no instances of high-risk statuses crossing the red line.

Table 7 Distribution of each safety situation level

Safety level	Node 1	Node 2	Node 3	Node 4
0	37 367	26 990	28 001	37 711
1	2 399	8 947	9 878	5 231
2	9 346	13 930	14 761	12 432
3	**11 368**	**10 613**	7 840	5 106

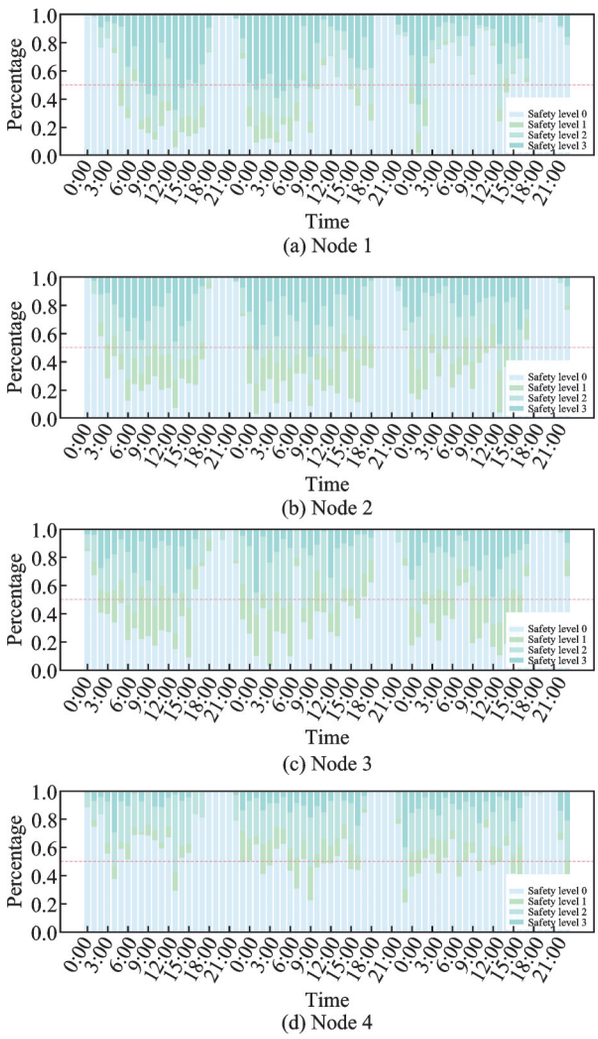

Fig.15 Percentage of safety levels per hour for the first three days across different sub-airspaces

Descriptive statistics for the hourly distribution of flight flow safety situation levels in different sub-airspaces are shown in Fig.16. This includes the mean average duration, standard deviation, 25th percentile, 75th percentile, median, and maximum proportion.

Fig.16(a) shows that the average proportion of

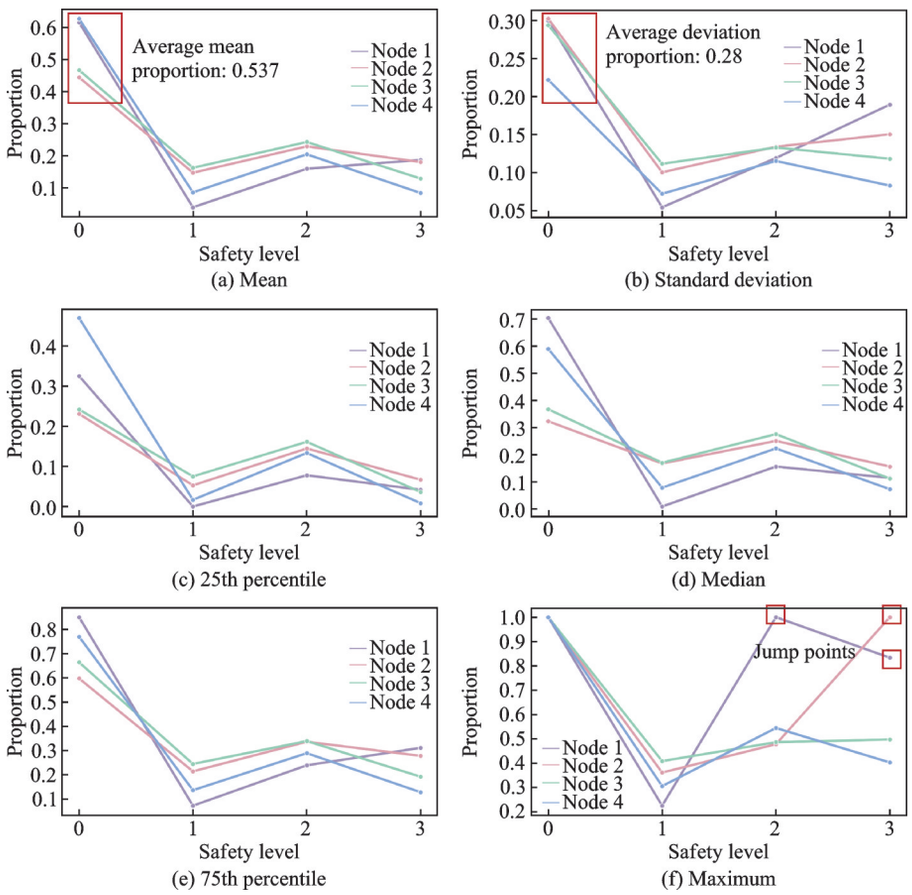

Fig.16 Descriptive statistics of the hourly distribution

Safety level 0 per hour is 0.537, which is the dominant situation, and Fig.16(b) indicates that its average standard deviation of 0.28 is significantly higher than other safety levels, with a wide range of fluctuations. This suggests there might be significant risk transitions during certain periods, meaning that even if the airspace has been relatively safe earlier, it cannot be taken lightly. Furthermore, Fig.16(f) reveals that there is a noticeable jump in the maximum values of Safety levels 2 and 3 at Node 1 and Node 2, indicating that high-risk situations may occur more irregularly and intensely at these nodes, reflecting the potential for more uncertain and rapidly changing risk factors at these locations.

(2) Duration of different safety situation levels

Descriptive statistics of the duration of different safety situation levels across various nodes are shown in Fig.17. This includes the mean average duration, standard deviation, 25th percentile, 75th percentile, median, and maximum proportion. Since the airspace is mostly in a quiescent state, the duration of Safety level 0 is much longer than that of other safety levels. Therefore, Fig.17 only displays the duration statistics for Safety levels 1, 2, and 3.

Fig.17(b) shows that high-risk levels among all node flight flows exhibit a larger standard deviation compared to low- and medium- risks, particularly at Node 1, where the standard deviation is significantly higher than those at other nodes, indicating a certain degree of variability. This suggests that the duration of high-risk states fluctuates greatly, reflecting instability and necessitating close monitoring. Fig.17(f) reveals that the maximum durations of high-risk states at Nodes 1 and 2 are 1 480 and 940, respectively, higher than those at other nodes, further indicating that Nodes 1 and 2 are more likely to face more complex risk situations.

In summary, the airspace overall shows a trend of gradually transitioning from low-risk situations to high-risk situations and then back to low-risk situations. Flight flows in Nodes 1 and 2 are more likely

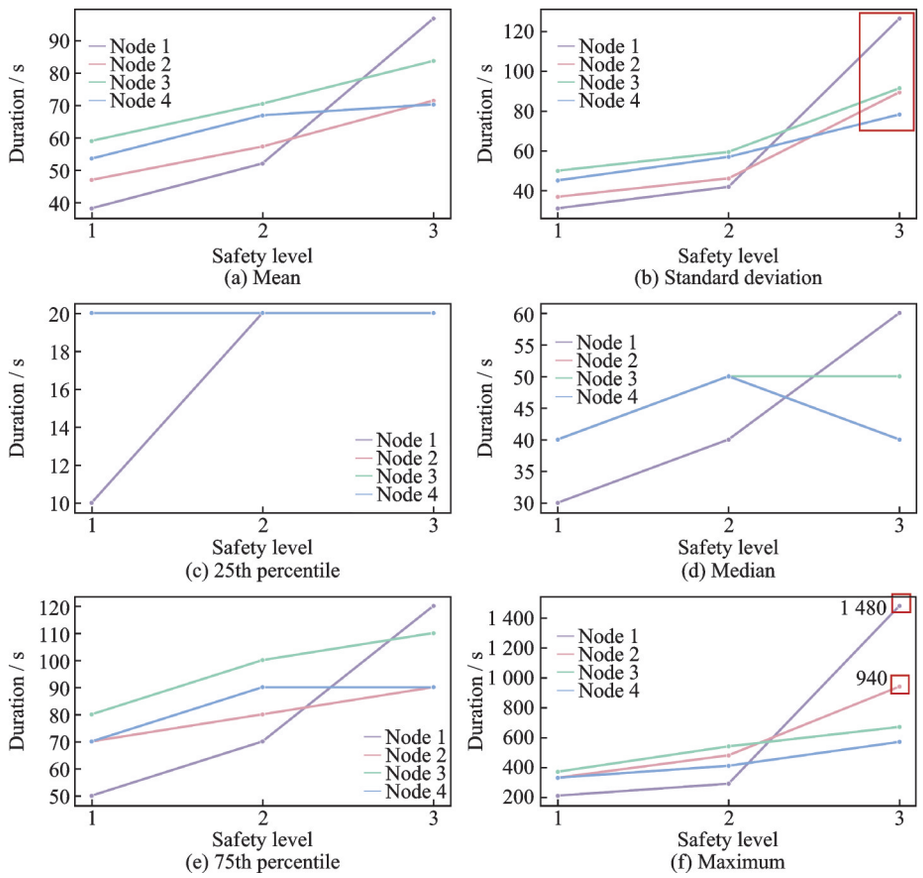

Fig.17 Descriptive statistics of the duration

to face complex risk scenarios, with the duration of each safety level being unstable and Safety level 3 showing the greatest fluctuation in duration. The air traffic control system should have adequate resilience to address and resolve emergencies.

(3) The potential temporal and spatial propagation paths of safety situation levels

This study employs cross-correlation to measure the similarity between time series at different time lags, aiming to uncover the potential temporal and spatial propagation paths of flight flow safety situation levels. The maximum cross-correlation lag time for each node's safety situation level is determined based on the connectivity between nodes, as illustrated in Fig.18.

Fig.18(a) shows that the safety situation level state of flight flows in Node 3 changes 34 time points earlier (approximately 5.7 min) than that in Node 2. Fig.18(b) indicates that Node 2 changes 28 time points earlier (approximately 4.7 min) than that in Node 1, and Fig.18(c) shows that Node 2 changes 12 time points earlier (approximately 2 min) than that in Node 4. From Fig.18(d), it is evident that Node 3 is the key node triggering safety state changes in other nodes and requires close monitoring to detect and prevent the spread of medium- and high-risk situations at the source. Since Node 2 is centrally located in the topology, acting as a hub connecting other nodes, it plays a crucial role in the transmission of safety situations. Therefore, it is essential to enhance monitoring and management of medium- and high-risk situations in Node 2's flight flows to interrupt the spread of risks along the transmission path.

3 Conclusions

We first extract a multidimensional safety situation assessment feature matrix centered on potential conflict risk, encompassing basic traffic flow parameters and aircraft maneuverability characteristics, providing a more comprehensive and accurate safety assessment perspective. Secondly, we propose a

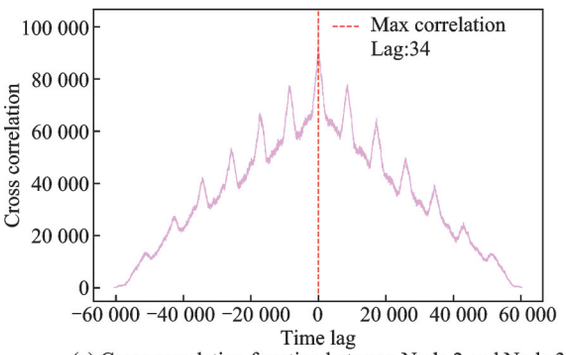

(a) Cross correlation function between Node 2 and Node 3

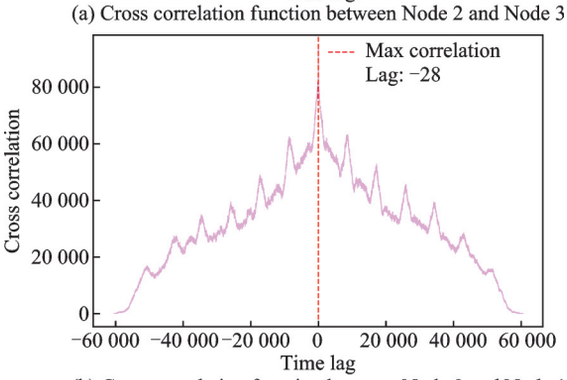

(b) Cross correlation function between Node 2 and Node 1

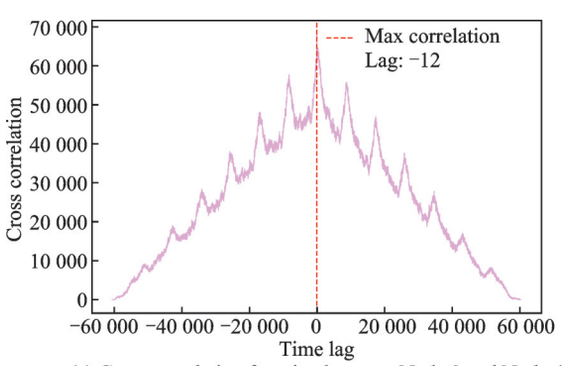

(c) Cross correlation function between Node 2 and Node 4

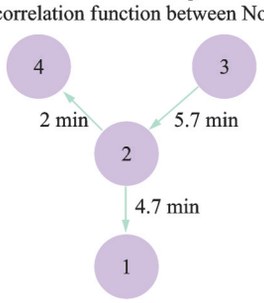

(d) The potential temporal and spatial propagation paths

Fig.18 The maximum cross-correlation lag time

deep clustering model with an added safety situation information capture layer to ensure that the encoded features can capture distinctive information about safety situations. Finally, we introduce a spatiotemporal graph convolutional neural network based on attention mechanism, comprehensively considering the spatiotemporal heterogeneity of safety situation to achieve precise prediction of safety situation levels.

According to experimental results, the following findings are drawn:

(1) Regarding air traffic situation recognition, a high silhouette coefficient does not necessarily indicate that the encoded (dimensionality-reduced) features can effectively capture distinctive information about the safety situation. This may lead to a mismatch between dimensionality-reduced features and the safety situation clustering goal. The proposed RADCM model not only more effectively partitions the dataset and generates more distinguishable clusters, but also ensures that the encoded features possess a certain capability to express safety risks.

(2) Concerning air traffic situation prediction, compared with traditional time series prediction models or simple neural networks, the ASTGCN model's comprehensive modeling capability in both space and time results in superior predictive performance, providing lower prediction errors and better generalization ability. This demonstrates the necessity of considering spatiotemporal heterogeneity in the field of air traffic prediction.

(3) High-risk situation usually occurs during critical phases of aircraft takeoff and landing, requiring more maneuver operations such as climbing, descending, and adjusting heading and speed, thereby increasing flight complexity and risk. These phases exhibit certain variability and instability, necessitating close monitoring.

(4) There is a general possibility of extreme events across all risk levels, which should be considered a key factor in risk management and emergency preparedness to ensure that the system has sufficient flexibility and resilience to handle sudden situations.

(5) Regarding safety risk management, strengthening the monitoring of flight flow risk origins (specifically in airspaces with high densities of arrival initiations and departure terminations) and optimizing transit management (particularly in areas near initial approach fix points) can significantly enhance the safety performance of the entire airspace system. This approach effectively reduces the likelihood of safety risks and diminishes their overall impact on the airspace network.

However, the proposed deep learning-based method for air traffic safety situation awareness in this study are only preliminary attempts. Future research will consider other factors affecting air traffic safety situations, such as emergency events and weather conditions.

References

[1] International Civil Aviation Organization (ICAO). 2020 safety report[R]. Montreal: ICAO, 2020.

[2] WU Dan. Analysis and application research of terminal area safety risk situation driven by data[D]. Tianjin: Civil Aviation University of China, 2022. (in Chinese)

[3] ENDSLEY M R. Design and evaluation for situation awareness enhancement[C]//Proceedings of the 32nd Human Factors Society Annual Meeting. Santa Monica, USA: Sage Publications, 1988.

[4] NUNEZ-PORTILLO J, VALENZUELA A, FRANCO A, et al. Predicting air traffic congestion under uncertain adverse weather[J]. Aerospace, 2024, 11(3): 240.

[5] TIAN W, ZHANG Y N, ZHANG Y, et al. A short-term traffic flow prediction method for airport group route waypoints based on the spatiotemporal features of traffic flow[J]. Aerospace, 2024, 11(4): 248.

[6] YU Z, SHI X, ZHANG Z. A multi-head self-attention transformer-based model for traffic situation prediction in terminal areas[J]. IEEE Access, 2023, 11: 16156-16165.

[7] LI B, LI Z, CHEN J, et al. MAST-GNN: A multimodal adaptive spatio-temporal graph neural network for airspace complexity prediction[J]. Transportation Research Part C: Emerging Technologies, 2024, 160: 104521.

[8] LI B, DU W, ZHANG Y, et al. A deep unsupervised learning approach for airspace complexity evaluation[J]. IEEE Transactions on Intelligent Transportation Systems, 2021, 23(8): 11739-11751.

[9] WANG H, XU X, ZHAO Y. Empirical analysis of aircraft clusters in air traffic situation networks[J]. Proceedings of the Institution of Mechanical Engineers, Part G: Journal of Aerospace Engineering, 2017, 231(9): 1718-1731.

[10] LIU F, LI J, WEN X, et al. Situation assessment of air traffic based on complex network theory and ensemble learning[J]. Applied Sciences, 2023, 13(21): 11957.

[11] ZHANG Honghai, LYU Wenying, WAN Junqiang, et al. Network modeling and evolution characteristics for air traffic risk situation in sectors[J]. Journal of Traffic Transportation Engineering, 2023, 23(1): 222-241. (in Chinese)

[12] WANG Hongyong, WEN Ruiying. Research on assessment of risk in air traffic situation based on complex network[J]. China Safety Science Journal, 2018, 28(5): 172-178.

[13] ZHANG X, ZHONG S, MAHADEVAN S. Airport surface movement prediction and safety assessment with spatial-temporal graph convolutional neural network[J]. Transportation Research Part C: Emerging Technologies, 2022, 144: 103873.

[14] WAN J Q, ZHANG H H, ZHANG Q Q, et al. Deep learning framework for forecasting en route airspace emissions considering temporal-spatial correlation[J]. Science of the Total Environment, 2023, 905: 166986.

[15] RA P, ERZBERGER H. Conflict probability estimation for free flights[J]. Journal of Guidance, Control, and Dynamics, 1997(3): 20.

[16] WANG H, SONG Z, WEN R, et al. Study on evolution characteristics of air traffic situation complexity based on complex network theory[J]. Aerospace Science and Technology, 2016, 58: 518-528.

[17] WU Minggong, YE Zelong, WEN Xiangxi, et al. Air traffic complexity recognition method based on complex networks[J]. Journal of Beijing University of Aeronautics and Astronautics, 2020, 46(5): 839-850. (in Chinese)

[18] WEN X, PENG Y, BI K, et al. Situation prediction of flight conflict network based on online fuzzy least squares support vector machine with optimal training set[J]. Journal of Computer Appllication, 2023, 43(11): 3632-3640. (in Chinese)

[19] LYU W, ZHANG H, WAN J, et al. Research on safety prediction of sector traffic operation based on a long short term memory model[J]. Applied Sciences, 2021, 11(11): 5141.

[20] BOUVEYRON C, BRUNET-SAUMARD C. Model-based clustering of high-dimensional data: A review[J]. Computational Statistics & Data Analysis, 2014, 71: 52-78.

[21] VON BORRIES G, WANG H. Partition clustering of high dimensional low sample size data based on p-values[J]. Computational statistics & data analysis, 2009, 53(12): 3987-3998.

[22] TRAN T N, WEHRENS R, BUYDENS L M. KNN-kernel density-based clustering for high-dimensional multivariate data[J]. Computational Statistics

& Data Analysis, 2006, 51(2): 513-525.
[23] LIN Y, ZHANG J W, LIU H. Deep learning based short-term air traffic flow prediction considering temporal-spatial correlation[J]. Aerospace Science and Technology, 2019, 93: 105113.
[24] YANG Wenda, WU Minggong, WEN Xiangxi, et al. Three-dimensional deterministic collision detection model based on velocity obstacle method[J]. Journal of Xihua University (Natural Science Edition), 2021, 40(6): 1-6. (in Chinese)
[25] HOU H, DING S, XU X. Research progress of deep clustering based on unsupervised representation learning[J]. Pattern Recognition and Artificial Intelligence, 2022, 35(11): 999-1014.
[26] TAO Wenbin, QIAN Yurong, ZHANG Yiyang, et al. Survey of deep clustering algorithm based on autoencoder[J]. Computer Engineering and Application, 2022, 58(18): 16-25. (in Chinese)
[27] VASWANI A, SHAZEER N, PARMAR N, et al. Attention is all you need[J]. Advances in Neural Information Processing Systems, 2017, 30: 5998-6008.
[28] DEFFERRARD M, BRESSON X, VANDERGHEYNST P. Convolutional neural networks on graphs with fast localized spectral filtering[C]//Proceedings of the 30th International Conference on Neural Information Processing Systems. [S.l.]: [s.n.],2016.
[29] HENAFF M, BRUNA J, LECUN Y. Deep convolutional networks on graph-structured data[EB/OL]. (2015-06-16). https://doi.org/10.48550/arXiv.1506.05163.

Acknowledgements The work was supported by the Chinese Special Research Project for Civil Aircraft (No.MJZ1-7N22) and the National Natural Science Foundation of China (No.U2133207).

Authors Mr. **DENG Cheng** received his B.S. degree from Civil Aviation Flight University of China in 2022. He is currently a postgraduate student in transportation engineering with College of Civil Aviation, Nanjing University of Aeronautics and Astronautics. His research interests include transportation planning and intelligent air transportation system.

Prof. **ZHANG Qiqian** received his M.S. and Ph.D. degrees in computer science and air traffic science from Nanjing University of Aeronautics and Astronautics in 2007 and 2015, respectively. His research interests include intelligent sensing of air traffic operation situation, transportation planning and intelligent air transportation system.

Author contributions Mr. **DENG Cheng** and Prof. **ZHANG Qiqian** designed the study, specialized in deep learning implementation, optimized algorithms, analyzed model performance, conducted the date analysis, interpreted the results and wrote the manuscript. Prof. **ZHANG Honghai** and Dr. **WAN Junqiang** ensured practical relevance, and validated model applicability. Mr. **LI Jingyu** contributed to data collection, preprocessing, and ensuring dataset accuracy and representativeness. All authors commented on the manuscript draft and approved the submission.

Competing interests The authors declare no competing interests.

(Production Editor: WANG Jing)

基于深度学习的终端区航班流运行安全态势感知方法

邓 成，张启钱，张洪海，万俊强，李靖宇

（南京航空航天大学民航学院空中交通管理系统全国重点实验室，南京 211106，中国）

摘要：安全是民航业的生命线，也是民航永恒的主题。本文面向终端区航班流，以空中交通复杂性及航空器潜在冲突关系为切入点，研究终端区航空器运行安全态势，提出了一种基于深度学习的终端区航班流安全态势感知方法。首先，提出更为全面和准确的安全态势评估特征；其次，构建一种添加安全态势信息捕捉层的深度聚类态势识别模型；最后，基于注意力机制构建时空图卷积神经网络的安全态势等级预测模型。通过真实数据集实验结果对本文所提方法进行评估，发现：(1) 本文所提模型在各方面性能上优于传统模型；(2) 所提态势识别模型能够确保编码特征可以捕捉到安全态势的区分性信息，增强模型的可解释性与识别任务的匹配性；(3)所提态势预测模型具有更优秀的空间和时间的综合建模能力。最后本文揭示了空中交通安全态势的时空演变特性，为空中交通安全管理提供参考。

关键词：空中交通；安全态势感知；深度学习；安全管理